Study of thermo-electrical and mechanical coupling during densification of a polycrystalline material using COMSOL

F. Mechighel[1,*,2,3], B. Pateyron[1] M. El Ganaoui[1] and M. Kadja[3]
[1]Université de Limoges, CNRS SPCTS UMR 6638, 87065 Limoges, France
[2]Université de Annaba, Département de Génie Mécanique, 23000 Annaba, Algérie
[3]Université de Constantine, Département de Génie Mécanique, 25000 Constantine, Algérie
*Corresponding author: Laboratoire SPCTS UMR 6638, 123 avenue Albert Thomas 87065 Limoges, email address: farid.mechighel@etu.unilim.fr

Abstract: Spark Plasma Sintering (SPS) is a promising rapid consolidation technique that allows a better understanding and manipulating of sintering kinetics and therefore makes it possible to obtain polycrystalline materials (ceramic or metallic) with tailored microstructures. A numerical simulation of the electrical, thermal and mechanical coupling during SPS is performed. Equations for conservation for energy, electrical charge and mechanical equilibrium are solved simultaneously. The strong coupling in term of temperature, on the thermal conductivity and electrical resistivity are considered.

Keywords: Numerical simulation, SPS, powder compacts ceramics, densification, sintering.

1. Introduction

Powder consolidation techniques such as hot pressing (HP) or hot isostatic pressing (HIP) often need a long heating period of up to several hours, leading to grain coarsening of the microstructure and preferred segregation of certain phases at grain boundaries [1]. In contrast, the SPS technique [2] has proven to be a rapid densification process that has the potential to minimize grain growth, which is crucial to achieving improved mechanical properties [3-5].

In SPS-type processes, the sintered part is produced from powders via the simultaneous application of pressure and external electric current and/or electric field.

The concept of compacting metallic materials to a relatively high density (> 90% of theoretical) by an electric discharge process was originally proposed by Inoue in the 1960s [6]. The first commercially operated spark plasma sintering (SPS) machine was developed, in 1990, with punches and dies made from electrically conductive graphite [7].

The SPS technique reposes on the application of a continuous pulsed Direct Current (DC), and a uni-axial load. The application of a strong electrical current promotes the activation of some diffusive processes which lead to densification of the powder (i.e. surface diffusion, grain boundary diffusion) [8, 9]. In the same manner, the stresses generated by the uni-axial load (especially the compressive hydrostatic stress) play the main role in the densification process during sintering.

The main objective of this work is the study of the role of key parameters in the SPS technique (i.e. the current density, applied load) on the distribution of the temperature and the stresses in the system. A numerical simulation of the electro-thermal and mechanical coupling, during SPS sintering, is performed. Results obtained may lead to optimizing die's geometry used in the SPS system.

2. General Considerations and Model Equations

2.1 SPS System

The SPS system is presented schematically in Fig. 1 [10]. The electrodes of electrical current (DC) alimentation are maintained at the temperature of *300 K*. The die, punches and spacers are usually in graphic. While; the electrodes are in copper. Thermo-physical and mechanical properties of all materials used in the SPS system are given in table 1 [10-11]. The samples used in this simulation are a ceramic as alumina and a metal as copper.

2.2 Mathematical Model

During SPS process, an electro-thermal and mechanical coupling may be presented. The origin of the electro-thermal coupling is firstly from the dependence of the electrical

conductivity on the temperature for all SPS components, also from Joule heating, generated by the electrical current.

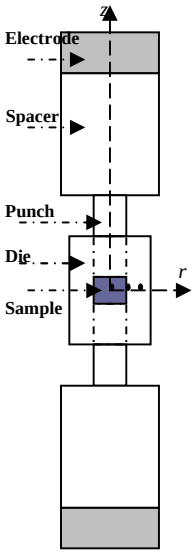

Dimensions:
Sample: diameter 0.019 m and length of 0.004 m
Electrode: diameter 0.076 m and length of 0.020 m
Die: diameter 0.044 m and length of 0.038 m
Punch: diameter 0.019 m and length of 0.04 m
Spacer: diameter 0.076 m and length of 0.038 m
Figure 1. The SPS system

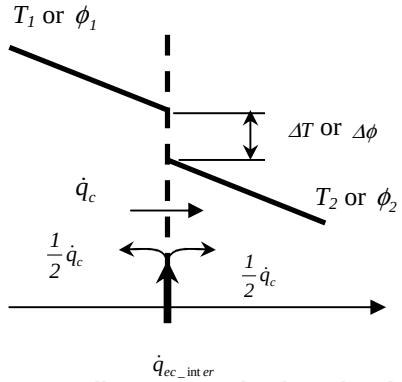

Figure 2. Illustration of the thermal and electrical contact resistances

2.2.1 Conservation of energy

Transient conductive heat transport (in the general form) for an axisymmetric model [12] is given by

$$\rho c_p \partial T/\partial t - \nabla\cdot(k\nabla T) = Q + \frac{h_{trans}}{dl}(T_{ext}-T) + \frac{C_{trans}}{dl}(T_{amb}^4 - T^4) \quad (1)$$

where ρ is the density [kg/m^3], c_p is the specific heat [J/kg K], k is thermal conductivity [W/m kg], Q is the heat source per volume unit (generation or absorption) [W/m^3], h_{trans} is the heat transfer coefficient relative to convection [W/kg m^2], C_{trans} is the heat transfer coefficient relative to radiation, T_{ext} is the external temperature [K], T_{amb} is the ambient temperature and *dl* is the thickness of the medium (material).

2.2.2 Conservation of electrical charge

In a conductive medium, the conservation of the electrical charge [12] is given by

$$\vec{\nabla}\cdot\vec{J} = -\partial q_{el}/\partial t \quad (2)$$

where $\boldsymbol{J}$ is the density of the electric field (A/m^2) q_{el} is the density of the electrical charge, we assume that the potential field is quasi-static which reduces the equation (2) to the following

$$\vec{\nabla}\cdot\vec{J} = 0 \quad (3)$$

The Ohm's law [12] allows us to express the current density as

$$\vec{J} = \sigma_{el}\vec{E} + \vec{J}_{el} \quad (4)$$

where σ_{el} is the electrical conductivity [S/m]; $\boldsymbol{E}$ is the electrical field [V/m] and $\boldsymbol{J_{el}}$ is the density of the external current generated [A/m^2], which is supposed zero in this study.

Joule's law allows us to express the volumetric heat source (Joule heating) per time unit as

$$Q = \dot{q} = \vec{J}\cdot\vec{E} = JE \quad (5)$$

The electrical field may, also, expressed as a gradient of the electrical potential ϕ as

$$\vec{E} = -\vec{\nabla}\phi \quad (6)$$

Therefore, equation (3) becomes

$$\vec{\nabla}\cdot\vec{E} = \vec{\nabla}\cdot(\sigma_{el}\vec{E}) = \vec{\nabla}\cdot(-\sigma_{el}\vec{\nabla}\phi) \quad (7)$$

For the axial symmetry case [12], the electrical potential is constant in the θ-direction and the potential field is tangent to *r-z* plane.

Substitution of equations (6 and 7) in (3) leads to

$$Q = (\vec{\nabla}\phi)\,\sigma_{el}(\vec{\nabla}\phi)$$

2.2.3 Equilibrium equation for the mechanical behaviour

We assume that the mechanical behaviour of the medium is quasi-static. Therefore, the equilibrium equation writes as

$$-\vec{\nabla}\cdot\{\sigma\}=\vec{F} \quad (8)$$

where $\{\sigma\}$ is the stress tensor and $\vec{F}$ the applied load. If the mechanical behaviour is supposed to be elastic, thus

$$\{\sigma\}=D\{\varepsilon\} \quad (9)$$

where D is elasticity matrix and $\{\varepsilon\}$ is the strain tensor.

With the thermal coupling, the displacement tensor due to thermal dilatation α writes as [12]

$$\left\{\varepsilon^{ther}\right\}=\left\{\alpha\left(T-T_{ref}\right)\quad \alpha\left(T-T_{ref}\right)\quad \alpha\left(T-T_{ref}\right)\right\}^{T}$$

where T_{ref} is the initial temperature of the medium.

As consequent $\{\sigma\}=D\left\{\varepsilon-\varepsilon^{ther}\right\}$

2.2.3 Thermal and electrical contact resistances

Heat may be provided at the surface of the medium by conduction thought parts (interfaces) which are in contact. When two surfaces are put in contact, irregularities held which do not allow a perfect contact. As consequent, the temperature and the potential will be discontinuous. In other word, a finite difference in the temperature and/or in the electrical potential is present up the contact (Fig.2).

The heat flux thought the contact interface [11] is given by

$$\dot{q}_c=h_g\left(T_1-T_2\right) \quad (10)$$

The current flux [11] is given by

$$J=S_g\left(\phi_1-\phi_2\right) \quad (11)$$

where h_g [W/K m^2] and S_g [W/m^2] are the thermal and electrical conductance, respectively; subscripts 1, 2 denote the two parts of the contact.

The thermal and electrical resistances are defined [11] by $R_c^{ther}=1/S_A h_g$ and $R_c^{el}=1/S_A s_g$, respectively, with S_A is the contact surface area.

In addition to the thermal and electrical potential loses, the heat flux is, also, discontinuous at the interface, this discontinuity is in form of heat lose by Joule heating due to the electrical resistivity of the contact [11]

$$\dot{q}_{ec\_inter}^{el}=J\left(\phi_1-\phi_2\right)=s_g\left(\phi_1-\phi_2\right)^2$$

As result, the heat flux on the contact surfaces (1) and (2) (Fig. 2) can be given by

$\dot{q}_{contact\,1}=q_c-0.5\,q_{ec\_inter}$, $\dot{q}_{contact\,2}=q_c+0.5\,q_{ec\_inter}$

where it is assumed the heat lose by Joule heating due to electrical resistance of the contact interface is eventually subdivided in two parts. Therefore, the flux difference through the contact interface is $\dot{q}_{contact\,2}-\dot{q}_{contact\,1}=\dot{q}_{ec\_inter}$

3. Results and Discussions

COMSOL 3.4 Multiphysics is used in the present numerical simulation.

In the simulation we consider the system SPS, at a DC current of 1000A and under a uniaxial load of 8.72 MPa. The thermal and electrical contact resistances are considered. Experiments [11] showed that the vertical contacts exhibit a higher contact resistance than the horizontal contacts (Fig. 2). The possible reason is that the load is directly applied on the horizontal contacts, which makes the horizontal contacts closer to perfect contact condition. The gap electric conductances (h_g) in horizontal and vertical directions are 1.25×10^7 and 7.5×10^6 (Ω^{-1} m^{-2}), respectively. While, the thermal conductances of the contact are taken in horizontal and vertical directions to be 2.4×10^3 and 1.32×10^3 Wm^{-2}K^{-1} , respectively. Therein [11], the sintering temperature and load applied are 1300°C and 15 MPa which close our values. Therefore we adopted these values in the actual study.

For the study of the effects of the discontinuities due to the contact resistances and mechanical friction on the electrical thermal and mechanical stresses fields, the following effects will be discussed:

3.1 The effect of resistivity of the sample on the distribution of electric and thermal fields

3.1.1 Distribution of electric and potential fields

Figs. 3 show the electric field in the system punches/die/alumina sample, and along the radial axis. Although the magnitude of the electric field varied during the process, the pattern of the electric field was practically independent of time.

Figs. 3a and b show the electric potential in the system and a long of radial axis, and they indicate clearly that a large potential difference

existed across the sample for alumina (insulating powder). There was a minor radial variation of electric potential (electric field) gradient (~40 V/m) in the alumina. This condition is often claimed to cause micro spark or plasma generated at particle contacts. The potential difference along the alumina sample is about 1% (i.e ~ 0.015 V) of the total voltage applied to the system (~ 2.30 V). For the copper, the potential difference accounted for only approximately <1% of the total voltage due to its low resistivity.

The information on electric field in the sample made it possible to examine the physical mechanisms that enhance the densification in SPS process (i.e. surface diffusion, grain boundary...). Even though several interpretations have been suggested [14], it is speculated that three major mechanisms are involved: (a) field emission; (b) voltage breakdown or discharge; and (c) thermal breakdown.

3.1.2 Current distribution in the system

Figs. 4 show the distribution of the density of the current in the system punches/die/sample and along the radial axis of the die/copper sample. The electric current density is higher in the punches and exhibited a maximum at the outside rim as a result of the large cross sectional area of the die. For a less electrically conductive sample (alumina), due to its high resistivity, practically all the current would be diverted into the die (not represented here). While, because the copper sample is with higher conductivity, the majority of the current crosses the copper.

Figs. 5 show the magnitude of the axial and the radial components of the electrical current in the punches/die/copper sample assembly at the steady state. Results showed that the direction of the current is mainly axial (*z*-direction). The only area, with a current flow in the radial direction (*r*-direction), is situated at top of the punch, and at the contact between the punch and the top surface of the die. The component of current density normal to the punch/die interface was continuous as required. There is no reason for the component of current density tangent to the interface to be continuous across the interface (see contours Figs. 5).

Comparison of the results of the present simulation with the results performed for the case where no resistance of contact are considered, see reference [15] reveals that the electrical contact resistances between the punches and the die have very strong role compared to the role of resistivity. Evidently, this conclusion concerns the actual die geometry chosen in the present study.

3.1.3 Joule heating distribution

Figs. 6 show that the amount of Joule heating in the punches is more about 100 times higher than the corresponding Joule heating inside the copper sample at the centre of the die. The electric conductivity of the sample did not affect significantly this heating. Because the majority of Joule heat generation occurred at the punches, the sample is indirectly heated by thermal conduction from the punches. The copper, also, exhibited a relatively great Joule heating, but its volume is small. Both electric current and Joule heat are only dependent on the local resistivity distribution in the system. Similar to electric current, Joule heating is highest at the ends of the punches due to the small diameter of the punches and the resulting high resistance. Joule heat is zero within the alumina and very small for the copper due to the small resistance of the copper.

3.1.4 Steady state temperature distribution

Without heat transfer (conduction, radiation), the temperature increase due to Joule heating was proportional to the local resistivity. Heat transfer modifies the initial temperature distribution. We assumed, here, that the graphite emissivety is 0.85, while those of copper and alumina are taken to be 1.

Figs. 7 show the temperature distributions within the punches/die/sample for the times (0, 10, 100, 200, 300, 400, 500 et 1000). As discussed above, regardless of the electrical conductivity of the sample, the punches generated the majority of the heat. The highest temperature in the system developed in the punches during the early heating stages. The heat was generated partially conducted into the sample and partially lost in the different components of SPS machine. As time increases, the temperature in the sample progresses due to thermal conduction from the punches. In addition, external surface radiation is a heat loss for the sample/die assembly. This pattern of heat flow resulted in a temperature gradient between the die surface and sample centre. For this

simulation the maximum predicted radial gradient is about 10°C (Fig. 7b). Significant temperature gradients were found in the radial direction for electrically conductive and insulating samples because of the heat flux pattern, i.e., conduction from the punch and heat loss through the die towards the surface of the die.

3.2 Friction Effects on the mechanical displacement and stresses fields

3.2.1 Mechanical displacement field

The mechanical displacements of the system are shown in Figs. 8. Fig. 8a shows the displacement in the radial direction for the case of alumina sample. In the punches/die/sample assembly, the radial displacement increases fairly uniformly with increasing radius, and hence the highest displacement occurs near the surface of the die. These radial displacements are due to the combination of the thermal expansion and a Poisson expansion due to the pressure applied in the *z*-direction. For the case of the copper sample displacements in r-direction are shown in Fig. 8b. Comparison of Figs. 8a and b shows different patterns of contour lines of radial displacements for alumina and copper samples (alumina results is not presented). The radial displacement in the copper case does not increase uniformly with the radius, as in the case of the alumina. Instead, the region of the copper in contact with the die wall (copper/graphite) is more displaced (deformed) than the regions where the punch is in contact with the die wall (graphite on graphite). In fact, the thermal dilatation coefficient for the copper is more greater than that of alumina, which promotes its deformation along of the die wall.

3.2.2 Stresses fields

Contour plots of radial, angular and vertical stresses in the radial plane for copper sample, at 1000A current input and under the applied pressure of 8.72 MPa, are presented in Figs. 9.

Larger differences in terms of stresses between the samples can be observed close to the sample. In the copper the distribution of the radial stress is not homogeneous. It corresponds to a compressive stress, in particular, in the contact zone of die/copper (Fig. 9a). While, in the alumina case, this stress is uniform and it is a tensile stress in the entire sample (it is not presented here due to lack of the space). For the angular stress, same remarks as those of the radial stress are observed (Fig. 9b). In contrast to the angular and radial stresses, the vertical stresses are compressive over the entire modelled section in both cases. The vertical stress is, also, uniform across the sample for alumina and non-uniform for copper. The stress nature (compression or tensile) is essentially due to the thermal expansion coefficient (although to the Young modulus) of the sample. The die in graphite of lower thermal expansion coefficient than that of the copper induces the compression of the copper during the temperature increase (Figs. 9). While, in the same conditions, alumina (with higher Young modulus and with approximately the same thermal expansion coefficient as that of the die in graphite) is subjected to tensile stresses.

5. Conclusion

The main conclusions of the present work are summarized as follows: (1) the temperature distribution is dependent on the conductivity of the sample. (2) Thermal gradients are not very significant in the modeled geometry and dimensions for either the copper or alumina system (<1.5% difference across the sample). (3) Displacements and stress distributions are dependent on sample properties (CTE and Young modulus).

6. References

1. M. N Rahamann, *Sintering of ceramics*, LRC Press Taylor & Francis Group, 2008
2. J.R., Groza, A. Zavaliangos, Sintering activation by external electrical field", *Mat. Sci. Eng.*, **A287**, 171-177 (2000)
3. K. Vanmeensel, A. Laptev, J. Hennicke, J. Vleugels, O. Van der Biest, Modelling of the temperature distribution during field assisted sintering", *ACTA Mat.*, **53**, 4379-4388 (2005)
4. Z. Shen, M. Nygren, Microstructural prototyping of ceramics by kinetic engineering: application of spark plasma sintering, *The Chem. Record*, **5**, 173-184 (2005)
5. L. Gao, Z.J. Shen, H. Miyamoto, M. Nygren, Superfast densification of oxide/oxide ceramic

composites. *J. Am. Ceram. Soc.*, **82**, 1061–1063 (1999)
6. K. Inoue, Electric Discharge Heat Treatment of Metals in Electrolytes, *US Patent* **3**,188-245 (1965)
7. O. Yanagisawa, T. Hatayama, K. Matsugi, Recent research on spark sintering, *Materia Japan*, **33**, 1489-1496 (1994)
8. Y. Zhou, K. Hirao, M. Toriyama, H. Tanaka, Very Rapid Densification of Nanometer Silicon Carbide Powder by Pulse Electric Current Sintering, *J. Am. Ceram. Soc.* **83**, 654–656 (2000)
9. L. Gao, J.S. Hong, H. Miyamoto, S.D.D.L. Torre, Bending strength and microstructure of Al2O3 ceramics densified by spark plasma sintering, *J. Euro. Ceram. Soc.*, **20**, 2149-2152 (2000)
10. X. Wang, S.R. Casolco, G. Xu, J.E. Garay, Finite element modeling of electric current-activated sintering: The effect of coupled electrical potential, temperature and stress, *Acta Materialia*, **55**, 3611–3622 (2007)
11. U. Anselmi-Tamburini, S. Gennari, J.E. Garay, Z.A. Munir, Fundamental investigations on the spark plasma sintering/synthesis process II. Modeling of current and temperature distributions, *Mater. Sci. Eng.* **A394**, 139–148 (2005)
12. COMSOL 3.4 manual
14. H. Braun, P. Herger, On the separation of the contributions of powder particle cores and intergranular contacts to the electric resistivity of compressed powder materials, *Materials Chemistry*, **7**, 787-802 (1982)
15. F. Mechighel, G. Antou, B. Pateyron, A. Maître, M. El Ganaoui, Simulation numérique du couplage électrique, thermique et mécanique lors du frittage 'flash' de matériaux céramiques et métalliques, *Congrès SFT (2008)*

10. Appendix

Table 1: Thermo-physical properties of the materials used in the simulation [11]

Alumina	
k	$\left(6.518\times10^{-7}+T\right)/\left(-6.696\times10^{-5}+8.175\times10^{-3}\,T\right)$
c_p	$\frac{7.77025\times10^{-3}T}{(249.4+T)}+\frac{790.15T}{249+T}+0.008T$
ρ_e	1×10^{8}
Copper	
k	$420.66+0.07\,T$
c_p	$355.3+0.1\,T$
ρ_e	$(5.5+0.038T)\times10^{-9}$
Graphite	
k	$65-0.017\,T$
c_p	$310.5+1.09\,T$
ρ_e	$21-3\times10^{-2}T+2\times10^{-5}T^2\quad-6.4\times10^{-9}T^3+7.8\times10^{-13}T^4$

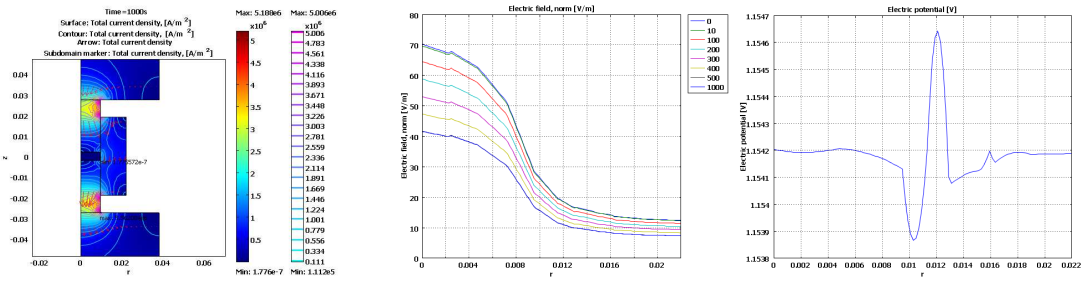

Figure 3. Electrical field in the Punches/Die/Sample (alumina) and along the radius of the assembly at various times.

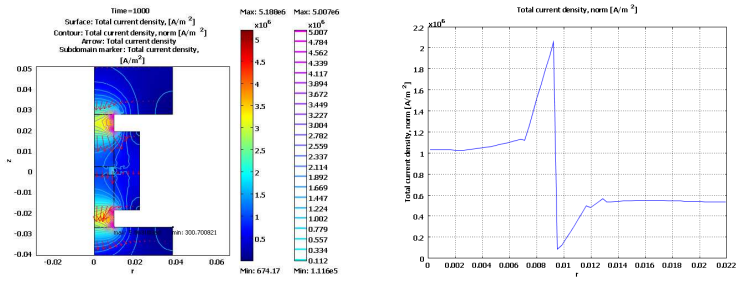

Figure 4. Current density distributions in the Punches/Die/Sample and along the radius of the assembly (copper).

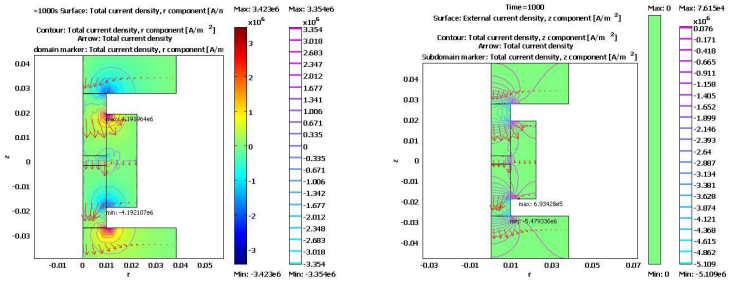

Figure 5. Current density components distributions in the Punches/Die/Sample assembly (copper).

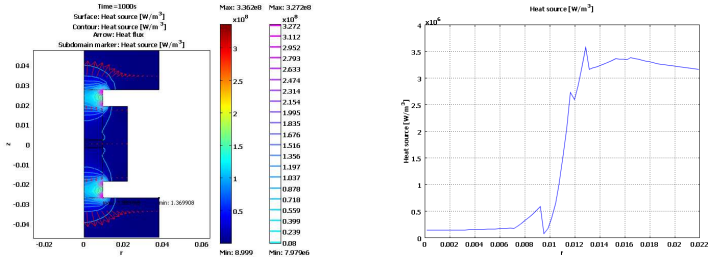

(a) *(b)*

Figure 6. Joule heating distributions in the Punches/Die/Sample and along the radius of the assembly (copper).

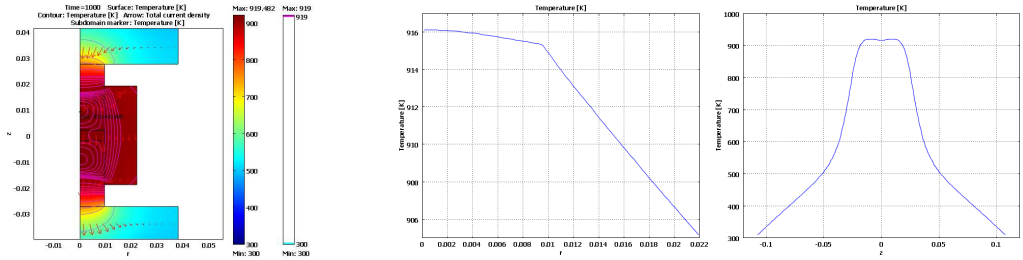

Figure 7. Temperature distributions in the Punches/Die/Sample (copper) (a) along the radius of the assembly (b) and along the axis of the SPS machine.

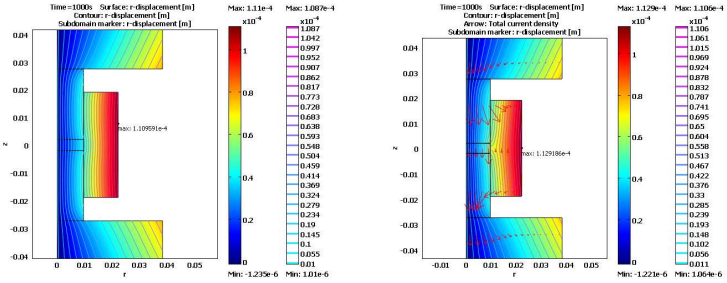

(a) alumina (b) copper

Figure 8. Radial displacement in the Punches/Die/Sample assembly for both alumina (a) copper (b).

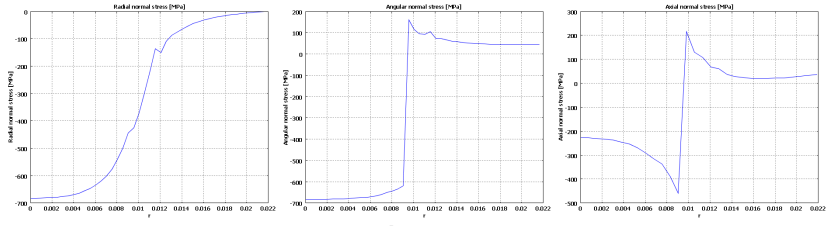

(a) (b) (c)

Figure 9. Stresses distributions along the radius of the assembly (copper sample) (a) radial, (b) angular and (c) axial.